Effectively Leveraging Solar Energy Through Persistent Dual Red Phosphorescence: Preparation, Characterization, and Density Functional Theory Study of $Ca_2Zn_4Ti_{16}O_{38}:Pr^{3+}$

ARTICLE *in* THE JOURNAL OF PHYSICAL CHEMISTRY C · APRIL 2010

Impact Factor: 4.77 · DOI: 10.1021/jp911885c

Effectively Leveraging Solar Energy through Persistent Dual Red Phosphorescence: Preparation, Characterization, and Density Functional Theory Study of $Ca_2Zn_4Ti_{16}O_{38}$:Pr^{3+}

Shixun Lian,*[†,‡] Yuan Qi,[†,‡] Chunying Rong,[†,‡] Liping Yu,[†,‡] Ailing Zhu,[†,‡] Dulin Yin,[†,‡] and Shubin Liu*[†,‡,§]

Key Laboratory of Resource Fine-Processing and Advanced Materials, Universities of Hunan Province, College of Chemistry and Chemical Engineering, Hunan Normal University, Changsha, Hunan 410081, China, Key Laboratory of Chemical Biology & Traditional Chinese Medicine Research (Ministry of Education), Hunan Normal University, Changsha, Hunan 410081, China, and Research Computing Center, University of North Carolina, Chapel Hill, North Carolina 27599-3420

Received: December 16, 2009; Revised Manuscript Received: March 2, 2010

To effectively leverage and convert cheap, abundant, and environmentally friendly solar energy is still an unaccomplished endeavor. In this work, we prepare and characterize the long-lasting red-light-emitting, single-phase $Ca_2Zn_4Ti_{16}O_{38}$ phosphor by the sol−gel method with nonstoichiometry or addition of H_3BO_3 as flux. Excitation and emission mechanisms are proposed and supported by the computational results from density functional theory. Phase identification of powders was performed by X-ray powder diffraction analysis, confirming the existence of single-phase $Ca_2Zn_4Ti_{16}O_{38}$ crystals in samples of every series. Unit cell parameters of the crystal were subsequently determined, together with its excitation spectra in the blue-green region with the maximum peak at 474 nm monitored by 644 nm light. The corresponding emission spectra showed a wide emission range with two narrow bands at 614 nm ($^1D_2 \rightarrow {}^3H_4$) and 644 nm ($^3P_0 \rightarrow {}^3F_2$) after the addition of H_3BO_3. If excited at 474 nm, the phosphor displays a superlong afterglow with the emission peak at 614 nm, enabling it to be a novel persistent red long phosphor for visible-light conversion. Luminescent properties of the phosphor were thoroughly examined. The mechanism of the dual persistence phosphorescence originated at 614 and 644 nm wavelengths induced by two separate kinds of doping defects was proposed. Density functional theory calculations under the periodic boundary condition provide insights about their excitation, emission, and long-lasting phosphorescence mechanisms.

1. Introduction

Solar energy is both endlessly abundant and environmentally green. To effectively leverage this clean and cheap energy source has been of tremendous recent research efforts in the literature. One of the proposals is to absorb and save the sunlight energy in daytime and then emit slowly in nighttime for illumination purposes through the long-lasting phosphor (LLP).[1] LLPs for two of the tricolor, blue and green, have long been available in the commercial market and already applied in many different fields. LLPs for the red color, the third of tricolor, are much harder to find and thus have attracted intensive research interests in the past decades, but so far, no satisfactory solution has been discovered.[2−4] Among the numerous red LLP candidates proposed, the oxidated phosphor $Ca_{0.8}Zn_{0.2}TiO_3$:Pr^{3+},Na^+ appears to be the most promising and suitable option because of its superior performance in phosphorescence persistence, chemical stability, low cost, and nontoxicity.[2,5−9] However, its excitation spectrum is in the ultraviolet region, leading to the limitation that the phosphor cannot be efficiently excited by the visible sunlight, and thus is ineffective in making use of and converting the solar energy.

Since 1997, Pr^{3+}-doped alkaline earth titanates (Pr-AET) have been the subject of many intensive studies.[2,5−10] Subsequent improvements in optical properties and proposals of the photoluminescence mechanism of $CaTiO_3$:Pr^{3+} in the solid state through changing material compositions have also been reported. So far, the mixed-phase phosphor of $CaTiO_3$ with $Ca_2Zn_4Ti_{16}O_{38}$ prepared with the nominal composition approach of $Ca_{0.8}Zn_{0.2}TiO_3$:Pr^{3+},Na^+ shows the most persistent phosphorescence in Pr-AET. It was suggested that Pr^{3+}-doped $Ca_2Zn_4Ti_{16}O_{38}$ played an important role in $Ca_{0.8}Zn_{0.2}TiO_3$:Pr^{3+},Na^+, though the specific mechanism of how the mixed-phase phosphor $Ca_{0.8}Zn_{0.2}TiO_3$:Pr^{3+},Na^+ functions is still unclear. In this paper, we report a new strategy to prepare the single-phase multititanate phosphor, $Ca_2Zn_4Ti_{16}O_{38}$ doped with Pr^{3+}, followed by detailed characterizations of its red LLP property. Finally, coupled with computational studies from density functional theory in the periodic boundary condition, the working mechanism for its persistent luminescence is proposed.

2. Experimental Section

2.1. Preparation of $Ca_2Zn_4Ti_{16}O_{38}$: Pr^{3+} Phosphors. Pr_6O_{11} was 99.99% in purity, and other starting materials were of analytical grade. $Ca(NO_3)_2 \cdot H_2O$ (A.R.), $Zn(NO_3)_2 \cdot 6H_2O$ (A.R.), $Ti(OC_4H_9)_4$ (A.R.), H_3BO_3 (A.R.), and $C_6H_8O_7 \cdot H_2O$ (A.R.) were used as raw materials. Solutions containing Ca^{2+}, Zn^{2+}, and Na^+ cations and H_3BO_3 were prepared by dissolving the stoichiometric solid $Ca(NO)_2$, $Zn(NO)_2$, NaCl, and H_3BO_3 in deionized water, respectively. Stoichiometric Pr_6O_{11} was dissolved in dilute HNO_3 under the vigorous stirring condition with the pH value

* To whom correspondence should be addressed. E-mail: lianshixun@yahoo.com.cn (S.X.L.), shubin@email.unc.edu (S.B.L.).
† College of Chemistry and Chemical Engineering, Hunan Normal University.
‡ Key Laboratory of Chemical Biology & Traditional Chinese Medicine Research (Ministry of Education), Hunan Normal University.
§ University of North Carolina.

10.1021/jp911885c
Published on Web 03/19/2010

TABLE 1: Optimized Preparation Conditions of Samples and the Results of X-ray Analysis (Calcining Time = 21 h)

	molar composition					X-ray analysis			
sample	Ca^{2+}	Zn^{2+}	Ti^{4+}	n_B/n_{Ti}	calcination temp (°C)	$CZT_{16}O$	CTO	ZTO	rutile
A0	2	4	15	0.0	950	√	√	√	
A1	2	4	15	0.3	1050	√			
A2	2	4	15	0.6	1050	√			√
A3	2	4	15	0.9	1050	√		√	√
A4	2	4	15	1.2	1050	√		√	√
A5	2	4	15	1.5	1050	√			√
B1	2	4	16	0.3	950	√			√
B2	2	4	16	0.6	950	√			√
B3	2	4	16	0.9	950	√			√
B4	2	4	16	1.2	950	√			√
B5	2	4	16	1.5	950	√		√	√
C1	2	4	16	0.1	950	√	√	√	√
C2	2	4.1	16	0.1	950	√		√	
C3	2	4.2	16	0.1	950	√			
C4	2	4.3	16	0.1	950	√		√	
C5	2	4.4	16	0.1	950	√		√	
D1	2	4	15.90	0.1	950	√	trace		
D2	2	4	15.95	0.1	950	√	√		
D3	2	4	16.00	0.1	950	√	√		
D4	2	4	16.05	0.1	950	√	√		
D5	2	4	16.10	0.1	950	√	√		

of the solution kept between 2 and 3. Four series of samples with varying metal cation compositions were prepared by the sol−gel method. Raw materials were added according to the ratio listed in Table 1.

Solutions containing a certain amount of Ca^{2+}, Zn^{2+}, Pr^{3+}, and Na^+ cations were mixed together to form a transparent solution (labeled as A). Under the constant stirring condition, stoichiometric $Ti(OC_4H_9)_4$ and H_3BO_3 solutions were dripped into a mixed solvent of glycol (30 mL) and citric acid (5.0 g) as a chelating agent for the metal ions to obtain a transparent solution (labeled as B). After that, solution A was added drop-by-drop to solution B at room temperature under continuous stirring until the formation of a pale yellow solution. Solvents were removed by heating in a distillation flask, and the color of the solution turned from pale yellow to bright yellow and finally to brown. As the solution became more viscous and resin-like, the excess solvent was removed at 100 °C in an oven. The temperature of the oven was elevated to 200 °C to obtain a dark solid dry gel. Once cooled to room temperature, the dried gel was then precalcined at 400 °C for 2 h to form brown-black precursor powders. After they were ground, the precursor powders were annealed at different temperatures for a period of time.

2.2. Characterizations. The precursor powders were examined using a Mettler Toledo TGA/SDTA 851^e derivatograph in air with the temperature range between 10 and 1200 °C, at the heating rate of 10 °C /min. The crystalline phase of the prepared samples was examined by X-ray diffractometry with Cu Kα radiation at 40 kV and 300 mA (Rigaku D/MAX-2500 X-ray diffractometer, Tokyo, Japan). Excitation and emission spectra of the samples were measured using an Hitachi F-4500 luminescence spectrofluorometer, equipped with a 175 W xenon lamp as an excitation source, a 400 V photomultiplier tube voltage, and a UV 350 nm filter. For the measurement of samples' decay curves, the photomultiplier tube voltage was changed to 700 eV and the response time kept at 0.004 s.

The thermoluminescence (TL) was measured using the spectrometer consisting of a linear heater and EG&G PAR optical multichannel analyzer (Department of Physics, Sun Yat-Sen University, China) with a heating rate of 5 K/s and a temperature range from 273 to 773 K. Before the measurement, powder samples were pressed into pellets about 5 mm in diameter and 0.5 mm in thickness, and then the phosphor samples were sealed in small polythene capsules to be irradiated for 5000 s with a Sr-90 source and the dose rate of 116 mGy/s at room temperature. All measurements except TL spectra were performed at room temperature.

2.3. Computational Details. Density functional theory calculations for the crystalline systems have been performed using the CASTEP module in the Material Studio program suite. The periodic boundary condition is used in all the calculations. Pseudopotentials were employed to represent core electrons, and plane-wave functions were used as basis sets. A 300 eV of the energy cutoff was used in the plane-wave basis expansion. The Perdew−Burke−Ernzerhof (PBE) exchange and correlation energy density functionals were employed in the DFT calculations in this study.

The cell parameters of the crystal structure for $Ca_2Zn_4Ti_{16}O_{38}$ and $CaTiO_3$ were obtained from the inorganic Crystal Structure Data database (coll code = 96258 for $CaTiO_3$[11] and 37025 for $Ca_2Zn_4Ti_{16}O_{38}$[12]). The unit cell of $Ca_2Zn_4Ti_{16}O_{38}$ and $CaTiO_3$ is shown in Scheme 1. To simulate the doping effect, we used the 2 × 2 × 2 supercell as the unit cell for $CaTiO_3$ and the 1 × 1 × 2 supercell for $Ca_2Zn_4Ti_{16}O_{38}$. A number of different doping sites have been systematically examined in the simulations. Single-point calculations with and without metal cation doping were performed to obtain electronic properties, such as the band structure, total and partial density of states, absorption spectra, etc. Calculations with optimized geometries give qualitatively similar results, as our tests have demonstrated.

3. Results and Discussion

3.1. TG−DTA Analysis. Figure 1 presents the combined thermogravimetric (TG) (red line) and differential thermal analysis (DTA) (green line) results of the polymeric precursor powder in the air atmosphere. It is found that the weight loss already starts at about 10 °C and becomes more significant until

SCHEME 1: Unit Crystal Cell of (a) $CaTiO_3$ and (b) $Ca_2Zn_4Ti_{16}O_{38}$

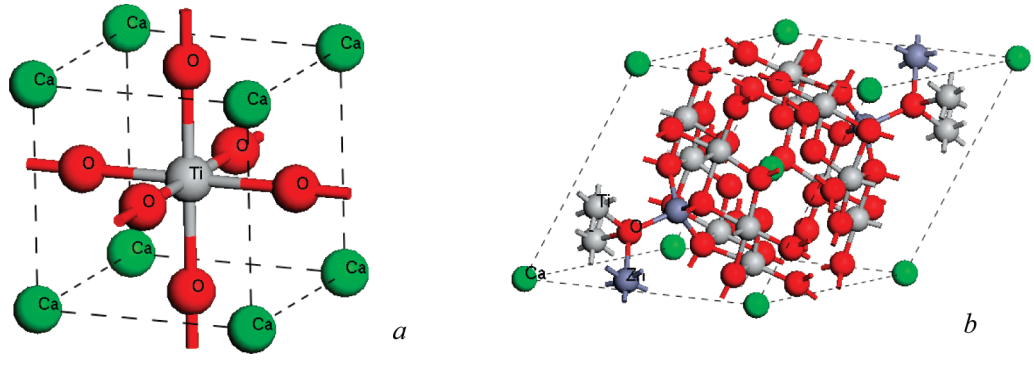

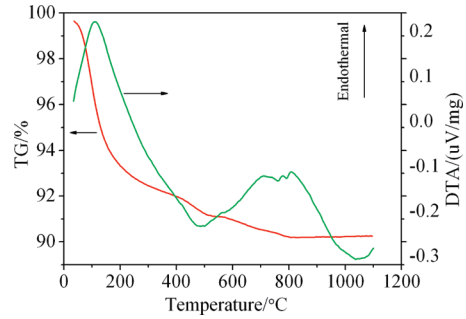

Figure 1. TG−DTA curves of the polymeric precursor powder.

200 °C, as evidenced from the sharp decline curve in the total weight, which is accompanied by an endothermic event in the DTA. This process is related to the water volatilization. Beyond 200 °C, only a slight weight change is observed until 500 °C, which is due to the breaking of the network structure and the decomposition of organic compounds. From 500 to 800 °C, the weight loss is accompanied again by an endothermic event, which can possibly be attributed to the phase formation and H_3BO_3 volatilization.

3.2. Structural Analysis. Since the discovery of $Ca_2Zn_4Ti_{15}O_{36}$ in 1981[13] and $Ca_2Zn_4Ti_{16}O_{38}$ in 1983,[12] much attention has been paid to understanding their structures and properties, especially their ceramic property.[14−23] Both materials have been used as microwave dielectric ceramics. $Ca_2Zn_4Ti_{15}O_{36}$ was not found to be the product when the exact ratio of elements, the stoichiometry of $n_{Ca}/n_{Zn}/n_{Ti} = 1:2:7.5$, was used for the raw materials, as reported by Bartram et al.[13] Gatehouse et al.[12] repeated the work of Bartram et al. and obtained $Ca_2Zn_4Ti_{16}O_{38}$ instead (with faint traces of $CaTiO_3$ and Zn_2TiO_4). Kim et al.[20,21] also reported that the single-phase $Ca_2Zn_4Ti_{15}O_{36}$ was not yielded through the solid-state reaction method and showed that the reaction proceeded as follows:

$$2CaO + 4ZnO + 15TiO_2 = 0.92Ca_2Zn_4Ti_{16}O_{38} + 0.16CaTiO_3 + 0.16Zn_2TiO_4$$

Meanwhile, we also found that, same as in the $Ca_2Zn_4Ti_{15}O_{36}$ case, the single-phase $Ca_2Zn_4Ti_{16}O_{38}$ crystal cannot be obtained if the stoichiometry of the starting raw materials is the same as that of the formula $Ca_2Zn_4Ti_{16}O_{38}$, $n_{Ca}/n_{Zn}/n_{Ti} = 1:2:8$.

Why cannot the single-phase $Ca_2Zn_4Ti_{15}O_{36}$ or $Ca_2Zn_4Ti_{16}O_{38}$ be synthesized by the high-temperature solid-state reaction in exact accordance with its stoichiometry? How does one overcome this problem to synthesize the desired product? In the present work, we report three different ways by the sol−gel method to subjugate the issue and successfully synthesize the single-phase $Ca_2Zn_4Ti_{16}O_{38}$. The crystal structure of the newly prepared phosphor has been corroborated by the XRD patterns and subsequent determination of the unit cell parameters. Luminescent properties of the phosphors obtained by three different approaches have also been compared.

Table 1 summarizes the preparation conditions as well as X-ray pattern data shown in Figure 2 for several series of samples. The XRD results of the samples can be indexed as rhombohedral $Ca_2Zn_4Ti_{16}O_{38}$ phase (JCPDS No. 85-1102) (marked as $CZT_{16}O$), perovskite $CaTiO_3$ phase (JCPDS No. 89-0056) (marked as CTO), cubic Zn_2TiO_4 phase (JCPDS No. 73-0578) (marked as ZTO), and rutile (JCPDS No. 71-0650). Zhao et al.[15−17] compared the difference between $Ca_2Zn_4Ti_{15}O_{36}$ and $Ca_2Zn_4Ti_{16}O_{38}$ and pointed out that XRD patterns of these two compounds are very much similar (JCPDS Nos. 34-0055 and 85-1102), except for the reflection lines around $2\theta \sim 13°$.

It can be seen from the XRD patterns in Figure 2 that the pure $Ca_2Zn_4Ti_{16}O_{38}$ phase (JCPDS No. 85-1102) is present in the powder samples, A1, C3, and D1. Comparing the preparation condition of samples A1, C3, and D1, we find that the pure phase $Ca_2Zn_4Ti_{16}O_{38}$ is yielded only under the condition that either Zn^{2+} is slightly higher or Ti^{4+} is slightly lower than what is required by stoichiometry. Also, when the molar ratio of Ca^{2+},

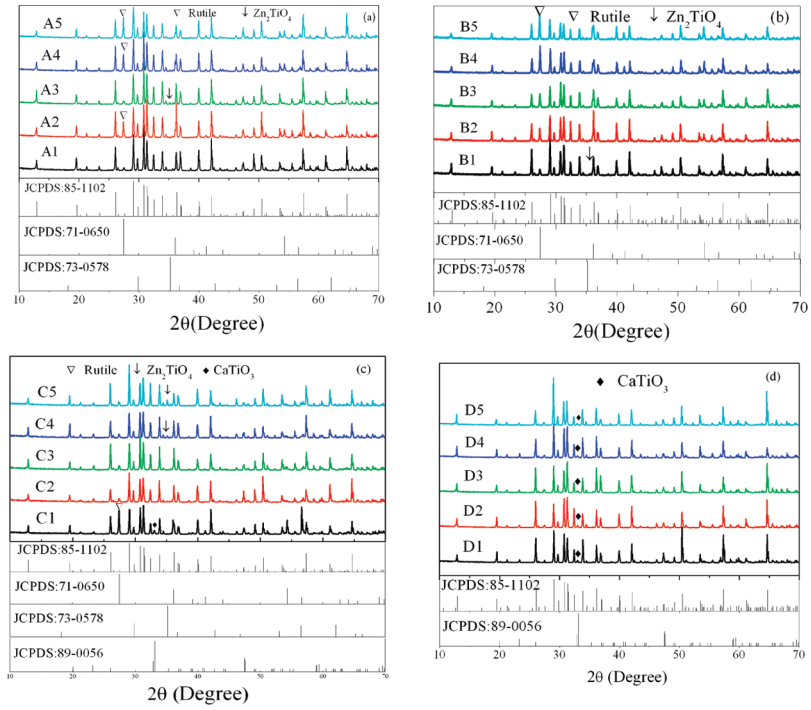

Figure 2. XRD patterns of the samples in Table 1.

TABLE 2: Unit Cell Data of the $Ca_2Zn_4Ti_{16}O_{38}$ Crystal Structure Prepared in This Work Compared with the Reference Values

sample	a (Å)	α (°)	volume (Å^3)
the reference values	9.024	68.65	651.82
A1	9.2139(7)	68.65(2)	653.93
C3	9.213(2)	68.630(2)	653.48
D1	9.2146(9)	68.66(2)	654.23

Zn^{2+}, and Ti^{4+} is 1:2:7.5, with the addition of H_3BO_3 (n_B/n_{Ti} = 0.3), the same product can be obtained. These results suggest that ZnO in the pseudoternary CaO−ZnO−TiO_2 system can easily be vaporized when heated at high temperature,[24−26] leading to the shortage of Zn^{2+} and thus the failure of preparing the single-phase $Ca_2Zn_4Ti_{16}O_{38}$ crystal, unless a certain amount of H_3BO_3 is added during the process to compensate for the loss. H_3BO_3 acts not only as flux but also as an impurity. B^{3+} cations enter into the crystalline lattice, substitute Ti^{4+}, and form the defect of B'_{Ti}. This is, in particular, the case when the preparation temperature is relatively high and more energy is provided for the B^{3+} cation substitution.

These XRD results show that at least three approaches are available to obtain single-phase $Ca_2Zn_4Ti_{16}O_{38}$ crystals: (1) with the molar ratio of $n_{Ca}/n_{Zn}/n_{Ti}$ = 2:4.2:16, deviated slightly from the required stoichiometry (ca. Zn^{2+} excess 5 mol % from C3) but with the addition of H_3BO_3 (n_B/n_{Ti} = 0.1) as flux; (2) with the molar ratio of $n_{Ca}/n_{Zn}/n_{Ti}$ = 2:4:15, with H_3BO_3 (n_B/n_{Ti} = 0.3) as flux; and (3) with the molar ratio of $n_{Ca}/n_{Zn}/n_{Ti}$ = 2:4:15.95, with H_3BO_3 (n_B/n_{Ti} = 0.1) as flux (plus a trace of $CaTiO_3$). No pure $Ca_2Zn_4Ti_{16}O_{38}$ can be obtained with the exact stoichiometriy of $n_{Ca}/n_{Zn}/n_{Ti}$ = 2:4:16, no matter how much H_3BO_3 is added (see D3 and B1−B5 in Table 1).

Shown in Table 2 are the crystal unit cell parameters of the three samples. These crystals belong to the rhombohedral, trigonal system, centrosymmetric space group $R\bar{3}$ (148) with a = 9.024 Å, α (°) = 68.65°, V = 651.82 Å^3, and Z = 1, according to the reference data.[12] This crystal is similar to the previously known structure of $Ca_2Zn_4Ti_{15}O_{36}$ in which Z = 3. The relationship between different samples through different approaches can be compared by the approximate parameters of their lattice listed in Table 2, indicating that the unit cell parameters of the $Ca_2Zn_4Ti_{16}O_{38}$ structure changed slightly with the varying preparation process, which is possibly resulted from the embedded B^{3+} cations. SEM results (Supporting Information, Figure S1) show that the samples are composed of aggregated particles ranging from 5 to 30 μm in size.

3.3. Spectra of $Ca_2Zn_4Ti_{16}O_{38}$:Pr^{3+},Na^+ Phosphor. Figure 3 shows the excitation (panels a and b) and emission (panels c and d) spectra of samples A1, C3, and D1. It is seen that each excitation spectrum mainly consists of three bands at 330, 380, and 474 nm, whereas the emission spectrum is a narrow band in the red region. Different samples give similar shapes and wavelengths in emission and excitation spectra but varied relative intensities.

There have already been many studies in the literature on the photoluminescence of Pr^{3+} in $MTiO_3$ (where M = Ca^{2+}, Sr^{2+}, Ba^{2+}) phosphors.[2,5−8,27−44] Different mechanisms of luminescence have been proposed. For the three excitation bands of $CaTiO_3$:Pr^{3+},Na^+, it is generally accepted that weak sharp lines between 450 and 495 nm are from the 4f → 4f transition of Pr^{3+} ions.[2,35,45,46] However, there is no consensus on how to assign the other two bands at 330 and 380 nm.[2,38,43,47] Recently, based on the relaxation trace of $CaTiO_3$:Pr^{3+} from the UV to red region,[35] Boutinand suggested that the band at 330 nm should be related to the transition from the valence band to the conduction band, O^{2-} 2p → Ti^{4+} 3d, and the band at 380 nm, instead of the prior assigned 4f → 5d transition of Pr^{3+}, was attributed to the charge transfer (CT) from Pr^{3+} to metal ions, Pr^{3+}/Ti^{4+} ↔ Pr^{4+}/Ti^{3+}. Zhang[43] assigned the excitation band at 265 nm to the 4f → 5d transition of Pr^{3+}. A shoulder peak at 265 nm had been observed when we examined the $Ca_{0.8}Zn_{0.2}TiO_3$:Pr^{3+},Na^+ phosphor.[22] Because the forbidden band of $CaTiO_3$ is 3.62 eV, the lowest absorption band will appear around 342.5 nm when the electron is excited from the valence band to the conduction band (O^{2-} 2p → Ti^{4+} 3d), which is in agreement with the excitation peak at 330 nm. The ability of Pr^{3+} to

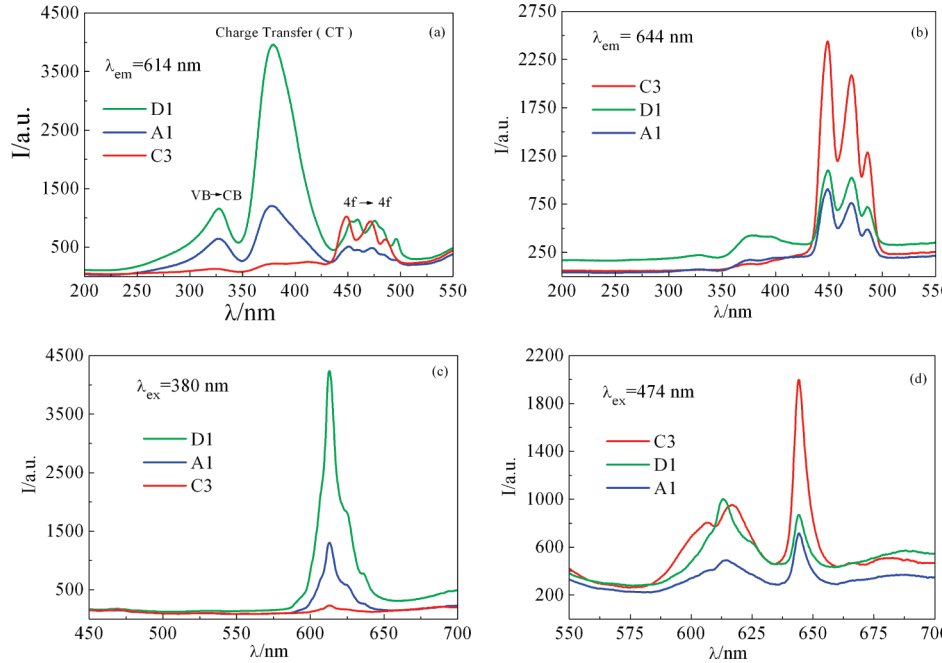

Figure 3. Excitation (a, b) and emission (c, d) spectra of samples A1, C3, and D1: (a) excitation spectra (monitoring wavelength = 614 nm), (b) excitation spectra (monitoring wavelength = 644 nm), (c) emission spectra (excited at 380 nm), and (d) emission spectra (excited by 474 nm).

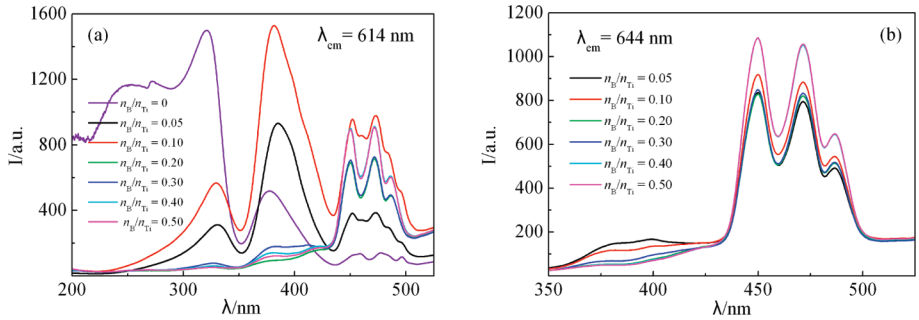

Figure 4. Excitation spectra of phosphors $Ca_2Zn_4Ti_{16}O_{38}$:0.6%Pr^{3+}, 0.6%Na^+ labeled as C3 in Table 1. ($n_B/n_{Ti} = 0$, calcined at 1050 °C, for 21 h; $n_B/n_{Ti} = 0.05-0.5$, calcined at 950 °C, for 21 h).

generate two photons for every absorbed photon has been known for quite some time.[48] Studies on Pr^{3+}-doped borates and other oxides[49] have shown that the biphononic luminescence of Pr^{3+} may occur if the lowest energy component of the 4f5d configuration is located above the $^1S_0$ energy level. Because of the phenomenon of phonon cascade, this kind of emission has never been detected in $CaTiO_3$:Pr^{3+}. Therefore, it is certain that the lowest level of the 5d energy levels split by Pr^{3+} is below the $^1S_0$ state, so the excitation bands between 200 and 300 nm should be assigned to the 4f → 5d transition of Pr^{3+}.

On the basis of the above analysis, the main excitation peak at 380 nm in $Ca_2Zn_4Ti_{16}O_{38}$:Pr^{3+},Na^+ can be attributed to the charge transfer from Pr to metal cation ($Pr^{3+}/Ti^{4+} \leftrightarrow Pr^{4+}/Ti^{3+}$). The minor peak at 330 nm be assigned to the transition from the valence band to the conduction band (VB → CB), O^{2-} 2p → Tl^{4+} 3d. The peaks between 450 and 495 nm are assigned to 4f → 4f transitions of Pr^{3+}. Because the crystal structures of $CaTiO_3$ and $Ca_2Zn_4Ti_{16}O_{38}$ are different, the amount of charge transfer from Pr to Ti cation ($Pr^{3+}/Ti^{4+} \leftrightarrow Pr^{4+}/Ti^{3+}$) varies, resulting in the red shift of the excitation peak from 380 to 394 nm.

Comparing the excitation spectra of $Ca_2Zn_4Ti_{16}O_{38}$:Pr^{3+},Na^+ with those of $CaTiO_3$:Pr^{3+}[9] and $Ca_{0.8}Zn_{0.2}TiO_3$:Pr^{3+},[22] we observe two apparent differences:[50] (1) The main excitation peak of both $CaTiO_3$:Pr^{3+} and $Ca_{0.8}Zn_{0.2}TiO_3$:Pr^{3+} is located at 330 nm, but that of $Ca_2Zn_4Ti_{16}O_{38}$:Pr^{3+},Na^+ is at 380 nm. (2) The excitation band between 450 and 495 nm is very weak for $CaTiO_3$:Pr^{3+} and $Ca_{0.8}Zn_{0.2}TiO_3$:Pr^{3+} samples, but it is strong and becomes the second strongest peak in the $Ca_2Zn_4Ti_{16}O_{38}$:Pr^{3+},Na^+ case. In addition, the peak at 330 nm shrinks to the smallest in $Ca_2Zn_4Ti_{16}O_{38}$:Pr^{3+},Na^+. These results illustrate that the 4f → 4f transition of Pr^{3+} in $Ca_2Zn_4Ti_{16}O_{38}$:Pr^{3+},Na^+ is enhanced, but the transition from the valence to conduction bands (O^{2-} 2p → Ti^{4+} 3d) and the charge transfer from Pr to Ti cations ($Pr^{3+}/Ti^{4+} \leftrightarrow Pr^{4+}/Ti^{3+}$) in $Ca_2Zn_4Ti_{16}O_{38}$:Pr^{3+},Na^+ is significantly reduced.

Upon excitation with light at 380 nm, all powder samples have demonstrated bright red emission at 614 nm, corresponding to the $^1D_2$ → $^3H_4$ transition of Pr^{3+} (Figure 3c). However, if excited by blue light at 474 nm, the phosphor displays two emission peaks in the red region (Figure 3d), with the first peak the same as the $^1D_2$ → $^3H_4$ transition of the Pr^{3+} ion and the second narrow band at 644 nm ascribed to the $^3P_0$ → $^3F_2$ transition of Pr^{3+}. Again, the excitation spectrum exhibits a strong excitation band in the range of 450−495 nm and does not show apparent excitation in the ultraviolet (200−430 nm) region when the phosphor is monitored by 644 nm light. These results indicate that the luminescence by Pr^{3+} is closely related to the host matrix.

3.4. Effect of H_3BO_3 on Afterglow Properties of Phosphors. Shown in Figure 4a,b are excitation spectra for the C3 sample monitored by 614 and 644 nm wavelengths, respectively. As shown in Figure 4a, monitored at 614 nm with the added H_3BO_3 n_B/n_{Ti} ratio less than 0.2, the main excitation peak of the samples is located around the near-ultraviolet region. With the concentration of H_3BO_3 increased, the excitation intensity at 377 nm as well as at blue and green regions is remarkably enhanced, with the band at 321 nm reduced and the shoulder near 250 nm completely disappeared. As shown in Figure 4b, monitored at 644 nm, excitation peaks of all samples are moved to the visible-light region (450−495 nm). The fact that all strong excitation bands are in visible areas has special significance in regard to our aim for the efficient sunlight leverage and conversion.

To study the decay behavior of Pr^{3+} luminescence in the phosphor samples A1, C3, and D1 in more detail, we measured the kinetic curve for the representative emission of Pr^{3+} $^1D_2-^3H_4$ and $^3P_0-^3F_2$ excited by UV (380 nm) and visible light, respectively, whose results are shown in Figure 5. For comparison purposes, the decay curve (Supporting Information, Figure S2) of $CaTiO_3$:0.2%Pr^{3+},0.2%Na^+ was also provided. The decay curves for the $^1D_2-^3H_4$ and $^3P_0-^3F_2$ emission of Pr^{3+} can be fitted by a double-exponential function, $I = A_1 \exp(-t/\tau_1) + A_2 \exp(-t/\tau_2)$, and the fitted results are listed in Table 3. Two lifetimes, τ_1 and τ_2, have been obtained for the emission of Pr^{3+}. The average lifetime for Pr^{3+} luminescence can be determined by the formula $\tau = (A_1\tau_1^2 + A_2\tau_2^2)/(A_1\tau_1 + A_2\tau_2)$. Also shown in Table 3 is the average lifetime of the 614 nm emission ($^1D_2-^3H_4$) of the C3 phosphor excited by 473 nm with the lasting time up to 257.61 ms, which is the longest among the three samples of $Ca_2Zn_4Ti_{16}O_{38}$:Pr^{3+},Na^+ phosphors. In contrast with the $CaTiO_3$:Pr^{3+},Na^+ phosphor, whose average lifetime of the 614 nm emission is only 175.68 ms, the new $Ca_2Zn_4Ti_{16}O_{38}$:Pr^{3+},Na^+ phosphor (e.g., sample C3) may be regarded as a novel persistent red phosphor candidate. The red phosphorescence of sample C3 excited by visible light can be seen in a dark surrounding by naked eyes for 30 min.

Because the three excitation bands at 330, 380, and 450−495 nm are related to the valence-to-conduction band transition (O^{2-} 2p → Ti^4 3d), charge transfer from Pr to Ti^4 metal ions ($Pr^{3+}/Ti^{4+} \leftrightarrow Pr^{4+}/Ti^{3+}$), and $^3H_4$ → $^1I_6$ and $^3H_4$ → ^3P_J (J = 0, 1, 2) transitions of Pr^{3+}, respectively, it is suggested that any factors perturbing the Ti−O configuration will affect the emission intensity and other luminescence-related properties of $Ca_2Zn_4Ti_{16}O_{38}$:Pr^{3+}. In general, the host matrix accepts photons and releases excited electrons, and the excited electrons are transferred to the luminescence center (Pr^{3+}) within the host lattice. The red luminescence at 614 and 644 nm is then emitted through Pr^{3+} $^1D_2$ → $^3H_4$ and $^3P_0$ → $^3F_2$ transitions. The direct relationship shown in Figure 4 between luminescent intensity and the amount of added H_3BO_3 suggests that B^{3+} ions have most likely entered into the host lattice and the crystal parameters were subsequently affected,

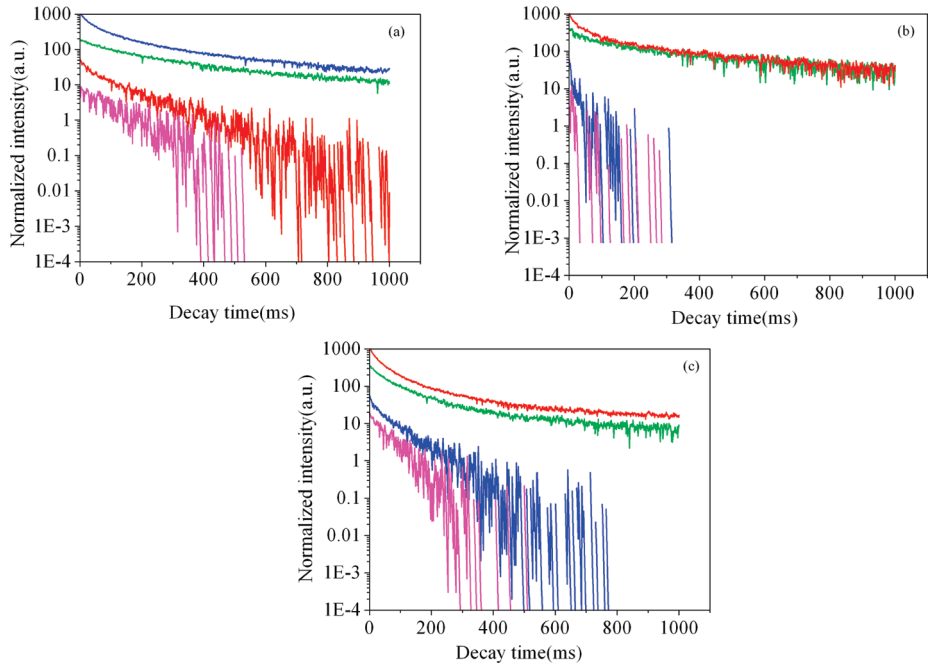

Figure 5. Decay curves (a−c) of the phosphors A1, C3, and D1, respectively: red line, monitoring wavelength at 614 nm, excited by 380 nm; green line, monitoring wavelength at 644 nm, excited by 380 nm; blue line, monitoring at 614 nm, excited by 473 nm; magenta line, monitoring at 644 nm, excited by 473 nm.

TABLE 3: Comparison of Phosphorescence Lifetimes of the Samples A1, C3, D1 and $CaTiO_3:Pr^{3+},Na^+$(CTP)

no.	λ_{ex} (nm), λ_{em} (nm)	A_1	τ_1	A_2	τ_2	τ
A1	380, 614	271.68	123.81	250.20	17.81	111.41
	380, 644	3812.36	193.54	6240.26	30.48	160.12
	473, 614	690.85	60.48	1094.14	272.73	246.66
	473, 644	20.46	0.77	71.14	100.29	100.07
C3	380, 614	823.95	23.78	391.55	219.38	183.05
	380, 644	69.04	4.65	16.01	33.23	22.47
	473, 614	258.04	278.68	228.72	28.98	257.61
	473, 644	3.05	19.64	3.05	19.64	19.64
D1	380, 614	3579.58	124.80	6593.64	24.03	98.42
	380, 644	293.67	76.30	242.15	11.09	69.32
	475, 614	1562.97	144.71	1907.46	33.53	120.20
	475, 644	55.58	11.82	132.30	60.39	56.70
CTP	380, 614	1374.88	197.57	1261.64	33.95	175.28

resulting in marked changes in the luminous intensity. On the basis of this reasoning, we propose that mild differences in the solid structure after the replacement of Ti^{4+} by B^{3+} are responsible for the enhancement of the luminous intensity.

3.5. Thermoluminescence. The thermoluminescence (TL) glow curve[31] is one useful way to determine the total number and activation energy of the trapping levels in materials.[26,51−54] A long-lasting phosphorescence requires the presence of abundant energy traps that are able to intercept free carriers, that is, electrons, holes, or their pairs, and to immobilize them for an appropriately long time. In particular, TL peaks close to (or above) room temperature are essential for the persistent luminescence. For this reason, the nature of trapped levels of the $Ca_2Zn_4Ti_{16}O_{38}:Pr^{3+},Na^+$ phosphor as well as the impact of the codoped B^{3+} cation on its thermoluminescence and persistent luminescence is carefully examined next.

The TL glow curves shown in Figure 6a reveal that several traps with rather different depths are present in the lightly doped species. These traps are able to intercept electrons and/or holes freed from the visible-light excitation. Some of the traps are relatively shallow (around 100 °C), whereas others are much deeper (200−350 °C). TL peak maxima (in degrees Celcius) and intensities of the TL glow curves of $Ca_2Zn_4Ti_{16}O_{38}:Pr^{3+},Na^+$ are summarized in Table 4. It clearly shows that there are two TL peaks in samples A1 and C3, but three TL peaks in sample D1.

Dorenbos[55] et al suggested that lanthanide energy levels and TL behaviors are strongly correlated for inorganic compounds and proposed an approach to predict what sites might act as an electron trap or a hole trap as well as what the depths of the traps are. According to this approach, the energy levels of Pr^{3+} in $Ca_2Zn_4Ti_{16}O_{38}$ prepared by different strategies were calculated and tabulated in Table 4. The energy levels of the traps present in these materials increase in the following order: $C_3 > A_1 > D_1$. There are two trapping levels in the materials that are suitable for long-lasting phosphorescence, but the deepest one (ca. 333 °C) is not appropriate for LLPs.

Shown in Figure 6b is the comparison of TL glow curves for two phosphors, $CaTiO_3:Pr^{3+},Na^+$ and $Ca_2Zn_4Ti_{16}O_{38}:Pr^{3+},Na^+$. It is seen that they have strikingly different activation energy levels as well as the total numbers of trapping levels. The TL glow curve of $CaTiO_3:Pr^{3+},Na^+$ exhibits one shallow peak at ca. 112 °C and one long tail in the higher temperature. For $Ca_2Zn_4Ti_{16}O_{38}:Pr^{3+},Na^+$, two peaks at 112 and 228 °C are observed. The first trap of $Ca_2Zn_4Ti_{16}O_{38}:Pr^{3+},Na^+$ in the low-temperature area is nearly identical to the first one of $CaTiO_3:Pr^{3+},Na^+$. These results imply that there are more and deeper defects in $Ca_2Zn_4Ti_{16}O_{38}:Pr^{3+},Na^+$, responsible for the observed persistent phosphorescence of $Ca_2Zn_4Ti_{16}O_{38}:Pr^{3+},Na^+$ in the red light region, whose decay is much slower than that of $CaTiO_3:Pr^{3+}$. More work on the detailed study of this property will be reported elsewhere.

3.6. Mechanism of the $Ca_2Zn_4Ti_{16}O_{38}:Pr^{3+},Na^+$ Phosphor. It is well-known that, to yield long-lasting luminescence, suitable trap energies must be existent. If a trap is too shallow, electrons will escape easily from it through thermal excitation, resulting in a short luminescence lifetime. On the other hand, if a trap is too deep, higher energy (temperature) is required for electrons

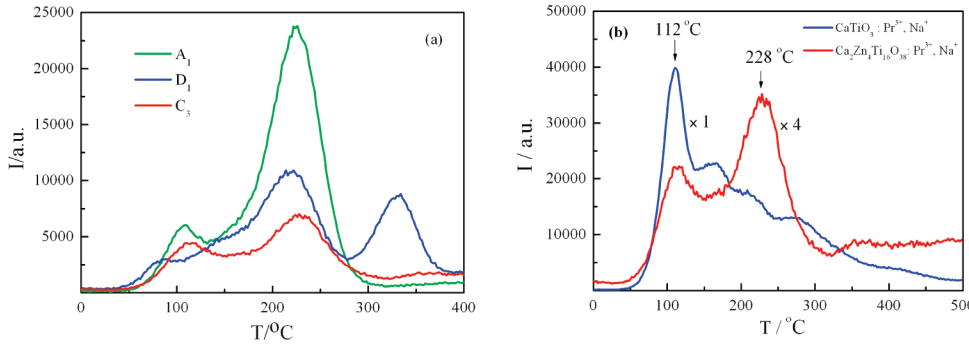

Figure 6. (a) Thermoluminescence glow curves of the phosphors $Ca_2Zn_4Ti_{16}O_{38}$:Pr^{3+},Na^+ prepared via nonstoichiometry: (green line), $n_{Ca}/n_{Zn}/n_{Ti}$ = 2:4:15, no H_3BO_3 (A1); (red line), $n_{Ca}/n_{Zn}/n_{Ti}$ = 2:4.2:16, n_B/n_{Ti} = 0.1 (C3); and (blue line), $n_{Ca}/n_{Zn}/n_{Ti}$ = 2:4:15.90, n_B/n_{Ti} = 0.1 (D1). (b) Comparison of the thermoluminescence glow curves of the phosphors, $CaTiO_3$:Pr^{3+},Na^+ and $Ca_2Zn_4Ti_{16}O_{38}$:Pr^{3+},Na^+ (C3).

TABLE 4: Peak Maxima (in Degrees Celcius) of the Thermoluminescence Glow Curves and the Trap Depth of $Ca_2Zn_4Ti_{16}O_{38}$:Pr^{3+},Na^+

sample	T_1 (°C)	E_1 (eV)	T_2 (°C)	E_2 (eV)	T_3 (°C)	E_3 (eV)
A1	109	0.764	225	0.996		
C3	117	0.780	228	1.002		
D1	87	0.720	220	0.986	333	1.212

stored in the trap to be excited, leading to undetectable or even no emission at room temperature.

Figure 7 shows the corresponding luminescence spectra, decay curves, point defects ($Pr^{\bullet}_{Ca}$ and $Pr^{\bullet}_{Zn}$), and energy levels of the Pr^{3+} ion in the $Ca_2Zn_4Ti_{16}O_{38}$:Pr^{3+},Na^+ phosphor. The band gap of $Ca_2Zn_4Ti_{16}O_{38}$ (sample C3) is around 3.80 eV in Figure 7a, according to the excitation spectrum (Figure 3a) and UV−visible absorption spectrum (Supporting Information, Figure S3). There are two bivalent cation positions, Ca^{2+} and Zn^{2+}, in the crystal that can be replaced by Pr^{3+} to form two different kinds of defects, one to replace Ca^{2+}, forming $Pr^{\bullet}_{Ca}$ and leading to 614 nm phosphorescence, and the other to take over Zn^{2+}, creating $Pr^{\bullet}_{Zn}$ and leading to 644 nm phosphorescence (see Figure 7b). Ti^{4+} cations can be substituted by B^{3+}, resulting in slight changes in lattice parameters. The higher the concentration of doped B^{3+} ions, the larger the extent of distortion and thus the stronger the $^3H_4 \rightarrow {}^1I_6 + {}^3P_J$ (J = 0, 1, 2) transition of Pr^{3+}. There exists experimental evidence that H_3BO_3 can enhance the 4f → 4f transition and give birth to a new $^3P_0 \rightarrow {}^3F_2$ transition (644 nm).[50] B^{3+} is doped into the lattice and forms the B'_{Ti} defect,[23,39] which is consistent with the findings that Al^{3+} ions and the like can significantly improve the luminescence of $SrTiO_3$:Pr^{3+} and $BaTiO_3$:Pr^{3+}.[7,32,56−58] The proposed mechanism of persistent luminescence for $Ca_2Zn_4Ti_{16}O_{38}$:Pr^{3+},Na^+ codoped by B^{3+} in Figure 7 summarizes excitation, emission, decay curves, and energy levels of the Pr^{3+} ion. The results reveal that the trap depth of the point defect $Pr^{\bullet}_{Zn}$ is deeper than that of $Pr^{\bullet}_{Ca}$, leading to the longer phosphorescence lifetime of $Ca_2Zn_4Ti_{16}O_{38}$:Pr^{3+},Na^+ than the $CaTiO_3$:Pr^{3+},Na^+ phosphor.

To better understand the luminescence mechanism of the phosphors and excitation processes, density function theory (DFT) has previously been employed in the literature.[26,59−63] Earlier computational results have shown that PDOS (partial density of states) can well account for the optical properties of $CaTiO_3$.[64] Computational results by Pontes[57] also showed that defect centers intrinsically existed in the amorphous $CaTiO_3$, forming various animated energy levels localized within the forbidden region. These energy levels serve as optical absorption centers and are responsible for the visible PL at room temperature. We utilized the Material Studio's CASTEP module and performed DFT calculations under the periodic boundary condition to obtain the band structure and total (DOS) and partial (PDOS) density of states for $CaTiO_3$:Pr^{3+} and $Ca_2Zn_4Ti_{16}O_{38}$:Pr^{3+} systems with and without doping effects. The calculated DOS and PDOS of $CaTiO_3$ and Pr-doped $CaTiO_3$ (CTO:Pr) are shown in Figure 8. As can be seen from the figure, O 2p and Ti 3d orbitals contribute mainly to the valence band (VB) and conduction band (CB), respectively. For $CaTiO_3$, the CB and VB are located at 1.84 and 0.05 eV, respectively, rendering the computed band gap of 1.79 eV, which is smaller than the experimental value of 3.5 eV. This discrepancy, however, is well-known in DFT because GGA/LDA functionals always underestimate the band gap owing to the discontinuity of the exchange-correlation potential. Our calculated band gap is, on the other hand, in good agreement with other theoretical results. For example, Saha[65] et al. obtained the band gap of 1.5 eV in LDA for the same system, and Wang[66,67] et al. reported the band gap of 1.85 eV in LDA and 1.95 eV in GGA.

For the doped $CaTiO_3$:Pr^{3+} system, due to the contributions from Pr 4f atomic orbitals, its valence and conduction bands are lowered to 1.17 and −0.55 eV, respectively, with the band gap slightly narrowed. These changes are in agreement with the experimental results, where the excited wavelength of the doped $CaTiO_3$ is found to have a red shift. In addition, comparing the total DOS between panels a and b in Figure 8, we find that there is an additional state in the band gap between the VB and CB of $CaTiO_3$: Pr^{3+}, which arises solely from Pr 4f orbital contributions, as shown in the PDOS of Figure 8b. This extra state in the band gap is the so-called defect energy level. According to the energy band theory and defect chemistry, due to the creation of this new state, excited elections from the VB to CB can hop to this trap state of Pr 4f orbitals, resulting in the increase of the capture transition time. That is, the long lasting phosphorescence is caused by the new Pr 4f band localized within the forbidden region of $CaTiO_3$'s band gap.

For $Ca_2Zn_4Ti_{16}O_{38}$, there are two possible ways to carry out the metal cation displacement: either Ca^{2+} or Zn^{2+} can be replaced by Pr^{3+}, denoted by $Pr^{\bullet}_{Ca}$ and $Pr^{\bullet}_{Zn}$, respectively. The total DOS of the undoped plus the two cases of the Pr^{3+}-doped $Ca_2Zn_4Ti_{16}O_{38}$ are shown in Figure 9a, from which we found that, because of the introduction of the doped cation, the CBs of both the doped $Pr^{\bullet}_{Ca}$ and $Pr^{\bullet}_{Zn}$ species are considerably lowered. In addition, the main difference between the undoped and doped species near the CB/VB regions is the appearance of a new DOS peak between CB and VB, same as in the case of $CaTiO_3$: Pr^{3+}. To probe the reason of the lowed CB of $Pr^{\bullet}_{Ca}$ and $Pr^{\bullet}_{Zn}$ and the nature of the new peak, shown in Figure 9b−d are the PDOS of $Ca_2Zn_4Ti_{16}O_{38}$ and the two doped counterparts. As exhibited in the plots, occupied p orbitals construct the VB, unoccupied d orbitals make up the CB, and Pr 4f orbitals in doped species

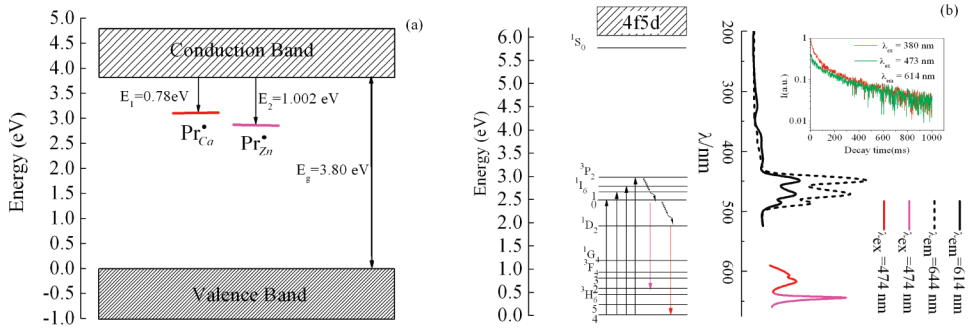

Figure 7. Energy band diagrams showing (a) level positions of Pr^{3+} ions inhabiting different crystal lattices in the band structure and (b) emission processes of $Ca_2Zn_4Ti_{16}O_{38}$:Pr^{3+},Na^+ phosphors (sample C3 in Table 1).

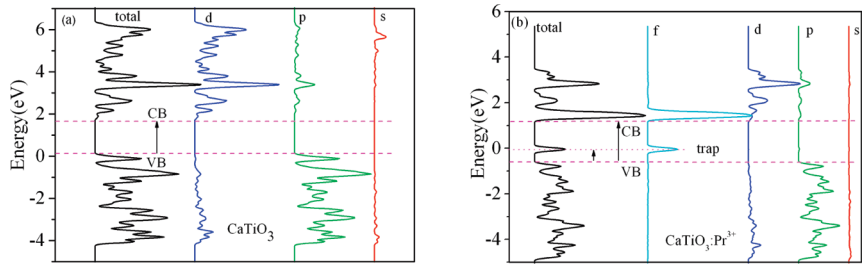

Figure 8. Total (DOS) and partial (PDOS) density of states of $CaTiO_3$ (a) and $CaTiO_3$:Pr^{3+} (b).

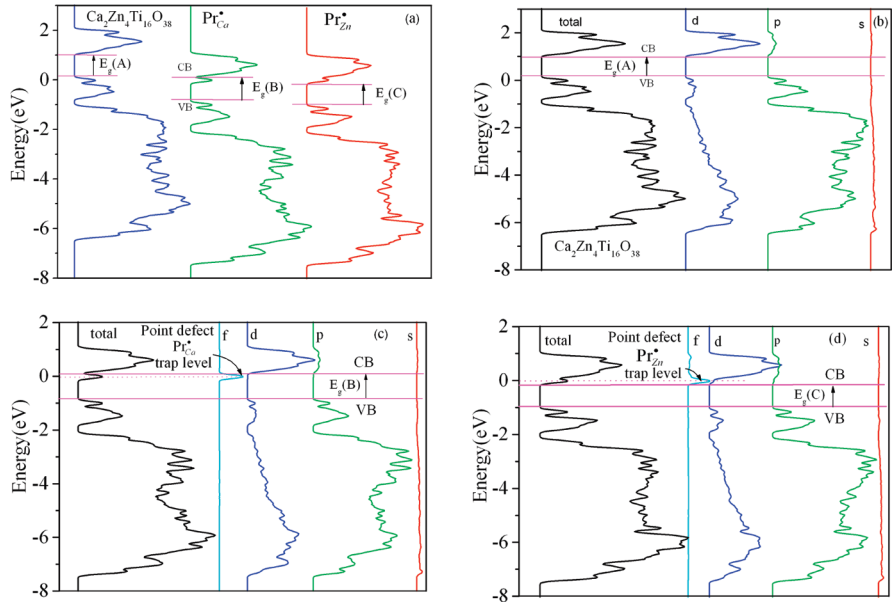

Figure 9. DOS and PDOS of undoped and doped $Ca_2Zn_4Ti_{16}O_{38}$ systems. (a) The total DOS for the pure and doped $Ca_2Zn_4Ti_{16}O_{38}$: $Ca_2Zn_4Ti_{16}O_{38}$ (blue), no doping; Ca−Pr (green), doped via Ca sites; and Zn−Pr (red), doping via Zn sites. (b) The PDOS of pure $Ca_2Zn_4Ti_{16}O_{38}$. (c) The PDOS for Pr replacing one Ca site in the $Ca_2Zn_4Ti_{16}O_{38}$ system. (d) The PDOS for Pr replacing one Zn in the $Ca_2Zn_4Ti_{16}O_{38}$ system.

are solely responsible for the appearance of the new peak between VB and CB. The introduction of this new band in the doped systems is the origin of the long-lasting phosphorescence of this system as it serves as the energy traps for emission in the bulk. The shrunken CB−VB band gap leads to the decreased excited energy and thus the red shift in the excitation wavelength, which is in good agreement with our above experimental results.

4. Concluding Remarks

In this work, our systematic study on the sol−gel preparation, structural and optical characterization, and computational chemistry study of the single-phased $Ca_2Zn_4Ti_{16}O_{38}$ phosphor is presented. Three approaches to prepare the single-phase crystal through additions of excess Zn^{2+}, deficient Ti^{4+}, and suitable addition of H_3BO_3 have been established. A slight departure from the stoichiometry of Zn^{2+} or Ti^{4+} is required to compensate for the loss of Zn^{2+} caused by volatilization in high-temperature solid-state reactions. The addition of a certain amount of H_3BO_3 is found to be beneficial for the pure phase formation and luminescence. This is because H_3BO_3 can act not only as flux but also as a doping impurity. The B^{3+} cation enters into the lattice, substitutes Ti^{4+}, forms B'_{Ti} defects, and leads to the improvement of crystalline perfection in $Ca_2Zn_4Ti_{16}O_{38}$:Pr^{3+} with a well-characterized visible-light excitation band at 474 nm and a super red persistence emission at 644 nm. The defect B'_{Ti} resulted in an increase in the energy transfer from the $Ca_2Zn_4Ti_{16}O_{38}$ host to the Pr^{3+} centers due to the transitions

$^3H_4 \rightarrow {}^1I_6$ and $^3H_4 \rightarrow {}^3P_J$ ($J = 0, 1, 2$) in Pr^{3+}. Our present crystal structure characterization and thermoluminescence studies have also revealed that the dual decay phosphorescence from 614 nm ($^1D_2 \rightarrow {}^3H_4$) and 644 nm ($^3P_0 \rightarrow {}^3F_2$) are induced by two defects ($Pr^{\bullet}_{Ca}$ and $Pr^{\bullet}_{Zn}$) created by the replacement of either Ca^{2+} or Zn^{2+} ions in $Ca_2Zn_4Ti_{16}O_{38}$ by Pr^{3+} ions. Density functional theory calculations under the periodic boundary condition for both undoped and doped $CaTiO_3$ and undoped and doped $Ca_2Zn_4Ti_{16}O_{38}$:Pr^{3+} systems provide insights about the excitation, emission, and long persistence mechanisms. Put together, the results from the present study suggest that $Ca_2Zn_4Ti_{16}O_{38}$:Pr^{3+} is one potential candidate for persistent red phosphors excited by the sunlight, moving us one step closer toward the ultimate goal of effectively leveraging the cheap, abundant, and environmentally green solar energy through the long-lasting phosphor.

Acknowledgment. This work was supported by the National Nature Science Foundation of China (Nos. 50772035, 20971042, and 20371017).

Supporting Information Available: SEM micrographs of samples A1, C3, and D1 (Figure S1); the decay curves of the phosphor $CaTiO_3$:Pr^{3+},Na^+(Figure S2); and the UV−visible absorption spectrum of sample C3 (Figure S3). This material is available free of charge via the Internet at http://pubs.acs.org.

References and Notes

(1) Matsuzawa, T.; Aoki, Y.; Takeuchi, N.; Murayama, Y. *J. Electrochem. Soc.* **1996**, *143*, 2670.
(2) Diallo, P. T.; Boutinaud, P.; Mahiou, R.; Cousseins, J. C. *Phys. Status Solidi A* **1997**, *160*, 255.
(3) Royce, M. R.; Matsuda, S.; Tamaki, H. U.S. Patent 5,650,094, July 22, 1997.
(4) Kinoshita, T.; Yamazaki, M.; Kawazoe, H.; Hosono, H. *J. Appl. Phys.* **1999**, *86*, 3729.
(5) Zhang, X.; Zhang, J.; Zhang, X.; Chen, L.; Lu, S.; Wang, X.-J. *J. Lumin.* **2007**, *122*−*123*, 958.
(6) Diallo, P. T.; Jeanlouis, K.; Boutinaud, P.; Mahiou, R.; Cousseins, J. C. *J. Alloys Compd.* **2001**, *323*−*324*, 218.
(7) Okamoto, S.; Kobayashi, H. *J. Appl. Phys.* **1999**, *86*, 5594.
(8) An, H.-K.; Kang, S.; Suh, K.-S. **2001**, *12*, 157.
(9) Pan, Y.; Su, Q.; Xu, H.; Chen, T.; Ge, W.; Yang, C.; Wu, M. *J. Solid State Chem.* **2003**, *174*, 69.
(10) Liu, X.; Jia, P.; Lin, J.; Li, G. J. *Appl. Phys.* **2006**, *99*, 124902.
(11) Vashook, V. V. L.; Knapp, M. *J. Alloys Compd.* **2003**, *354*, 13.
(12) Gatehouse, B. M.; Grey, I. E. *J. Solid State Chem.* **1983**, *46*, 151.
(13) Bartram, S. F.; Foss, W. M. *J. Am. Ceram. Soc.* **1981**, *64*, 80.
(14) Haranath, D.; Khan, A. F.; Chander, H. *J. Phys. D: Appl. Phys.* **2006**, *39*, 4956.
(15) Zhao, F.; Yue, Z.; Lin, Y.; Gui, Z.; Li, L. *Ceram. Interfaces* **2006**.
(16) Zhao, F.; Yue, Z. X.; Lin, Y. Z.; Gui, Z. L.; Li, L. T. *Ceram. Interfaces* **2007**, *33*, 895.
(17) Zhao, F.; Yue, Z. X.; Gui, Z. L.; Li, L. T. *J. Electroceram.* **2007**, *21*, 120.
(18) Yang, H. K.; Shim, K. S.; Jeong, Y. R.; Moon, B. K.; Choi, B. C.; Jeong, J. H.; Bae, J. S.; Yi, S. S.; Kim, J. H. *Thin Solid Films* **2008**, *516*, 1613.
(19) Pang, L. X.; Wang, H.; Yue, H. C.; Zhou, D.; Yao, X. *J. Mater. Sci.* **2008**, *20*, 528.
(20) Kim, H. T.; Byu, J. D.; Kim, Y. *Mater. Res. Bull.* **1998**, *33*, 963.
(21) Kim, H. T.; Byun, J. D.; Kim, Y. *Mater. Res. Bull.* **1998**, *33*, 975.
(22) Lian, S.; Zuo, C.; Yin, D.; Li, C.; Zhang, H. *J. Rare Earths* **2006**, *24*, 29.
(23) Wanjun, T.; Donghua, C. *J. Am. Ceram. Soc.* **2007**, *90*, 3156.
(24) Bassett, W. H. Zinc Losses. *J. Ind. Eng. Chem.* **1912**, *4*, 164.
(25) Anthrop, D. F.; Searcy, A. W. *J. Phys. Chem.* **1964**, *68*, 2335.
(26) Lian, S.; Rong, C.; Yin, D.; Liu, S. B. *J. Phys. Chem. C* **2009**, *113*, 6298.
(27) Itoh, S.; Toki, H.; Tamura, K.; Kataoka, F. *Jpn. J. Appl. Phys.* **1999**, *38*, 6387.
(28) Byun, J.-W.; Lee, B.-K.; Kim, D.-K.; Kang, S.-G.; Kang, S.-Y.; Suh, K.-S. *Mater. Res. Soc. Symp. Proc.* **2001**, *667*, G3.7.1.
(29) Kim, J. Y.; Jeon, D. Y.; Kang, S.-G.; Kang, S.-Y.; Suh, K.-S. *Mater. Res. Soc. Symp. Proc.* **2001**, *667*, G3.7.1.
(30) Okamoto, S. *Appl. Phys. Lett.* **2001**, *78*, 655.
(31) Kim, K. H.; Park, J. K.; Kim, C. H.; Park, H. D.; Chang, H.; Choi, S. Y. *Ceram. Interfaces* **2002**, *28*, 29.
(32) Okamoto, S.; Yamamoto, H. J. *Appl. Phys.* **2002**, *91*, 5492.
(33) Jia, W.; Xu, W.; Rivera, I.; Pérez, A.; Fernández, F. *Solid State Commun.* **2003**, *126*, 153–157.
(34) Kang, S.-Y.; Byun, J.-W.; Kim, J. Y.; Suh, K.-S.; Kang, S.-G. *Bull. Korean Chem. Soc.* **2003**, *24*, 566.
(35) Boutinaud, P.; Pinel, E.; Dubois, M.; Vink, A. P.; Mahiou, R. *J. Lumin.* **2005**, *111*, 69.
(36) Boutinaud, P.; Pinel, E.; Oubaha, M.; Mahiou, R.; Cavalli, E.; Bettinelli, M. *Opt. Mater.* **2006**, *28*, 9.
(37) Boutinaud, P.; Tomasella, E.; Ennajdaoui, A.; Mahiou, R. *Thin Solid Films* **2006**, *515*, 2316.
(38) Jiaa, W.; Jia, D.; Rodriguez, T.; Evans, D. R.; Meltzer, R. S.; Yen, W. M. *J. Lumin.* **2006**, *119*−*120*, 13.
(39) Tang, J.; Yu, X.; Yang, L.; Zhou, C.; Peng, X. *Mater. Lett.* **2006**, *60*, 326.
(40) Zhang, X.; Zhang, J.; Zhang, X.; Chen, L.; Luo, Y.; Wang, X.-j. *Chem. Phys. Lett.* **2007**, *434*, 237.
(41) Zhang, X.; Zhang, J.; Zhang, X.; Wang, M.; Zhao, H.; Lu, S.; Wang, X.-j. *J. Phys. Chem. C* **2007**, *111*, 18044.
(42) Boutinaud, P.; Pinel, E.; Mahiou, R. *Opt. Mater.* **2008**, *30*, 1033.
(43) Zhang, X.; Zhang, J.; Ren, X.; Wang, X.-J. *J. Solid State Chem.* **2008**, *181*, 393.
(44) Zhang, X.; Zhang, J.; Wang, M.; Zhang, X.; Zhao, H.; Wang, X.-J. *J. Lumin.* **2008**, *128*, 818.
(45) Derén, P. J.; Pązik, R.; Stręk, W.; Boutinaud, P.; Mahiou, R. *J. Alloys Compd.* **2008**, *451*, 595.
(46) Kyômen, T.; Sakamoto, R.; Sakamoto, N.; Kunugi, S.; Itoh, M. *Chem. Mater.* **2005**, *17*, 3200.
(47) Dereń, P. J.; Mahiou, R.; Pązik, R.; Lemanski, K.; Stręk, W.; Boutinaud, P. *J. Lumin.* **2008**, *128*, 797.
(48) Shi, W. S.; Chen, Z. H.; Liu, N. N.; Lu, H. B.; Liang, Z. Y.; Cui, D. F.; Yang, G. Z. *Sci. China, Ser. A* **2000**, *43*, 527–532.
(49) Setlur, A. A.; Srivastava, A. M. *Opt. Mater.* **2007**, *29*, 1647.
(50) Kalabukhov, A.; Gunnarsson, R.; Börjesson, J.; Olsson, E.; Claeson, T.; Winkler, D. *Phys. Rev. B* **2007**, *75*, 121404(R).
(51) Rieke, J. K.; Daniels, F. *J. Phys. Chem.* **1957**, *61*, 629.
(52) Clabau, F.; Rocquefelte, X.; Jobic, S.; Deniard, P.; Whangbo, M. H.; Garcia, A.; Mercier, T. L. *Chem. Mater.* **2005**, *17*, 3904.
(53) Kudo, A. *Chem. Mater.* **1997**, *9*, 664.
(54) Schipper, W. J.; Blasse, G.; Leblans, P. *Chem. Mater.* **1994**, *6*, 1784.
(55) Dorenbos, P.; Bos, A. J. J. *Radiat. Meas.* **2008**, *43*, 139–145.
(56) Okamoto, S.; Kobayashi, H.; Yamamoto, H. *J. Electrochem. Soc.* **2000**, *147*, 2389.
(57) Okamoto, S.; Tanaka, S.; Yamamoto, H. *J. Lumin.* **2000**, *87*−*89*, 577.
(58) Okamoto, S.; Yamamoto, H. *J. Lumin.* **2003**, *102*−*103*, 586.
(59) Pontes, F. M.; Pinheiro, C. D.; Longo, E.; Leite, E. R.; Lazaro, S. R.; Varela, J. A.; Pizani, P. S.; Boschi, T. M.; Lanciotti, F. *Mater. Chem. Phys.* **2002**, *78*, 227.
(60) Longo, E.; Orhan, E.; Pontes, F. M.; Pinheiro, C. D.; Leite, E. R.; Varela, J. A.; Pizani, P. S.; Boschi, T. M.; Lanciotti, F., Jr.; Beltran, A.; Andres, J. *Phys. Rev. B* **2004**, *69*, 125115.
(61) Samantaray, C. D.; Sim, H.; Hwang, H. *Microelectron. J.* **2005**, *36*, 725.
(62) Ullrich, C. A. *J. Chem. Theory Comput.* **2009**, *5*, 859.
(63) Tamar, S.; Leeor, K.; Roi, B. *J. Am. Chem. Soc.* **2009**, *131*, 2818.
(64) Ueda, K.; Yanagi, H.; Hosono, H.; Kawazoe, H. *J. Phys.: Condens. Matter* **1999**, *11*, 3535.
(65) Saha, S.; Sinha, T. P.; Mookerjee, A. *Eur. Phys. J. B* **2000**, *18*, 207.
(66) Yang, K.; Wang, C.-L.; Li, J.-C.; Zhang, C.; Wu, Q.-Z.; Zhang, Y.-F.; Yin, N.; Liu, X.-Y. *Chin. Phys.* **2006**, *15*, 1580.
(67) Wang, Y. X.; Arai, M.; Sasaki, T.; Wang, C. L. *Phys. Rev. B* **2006**, *73*, 035411.

JP911885C